Use of 'velocity projection' to estimate the variation of sea-surface height from HF Doppler radar current measurements

G.O. Marmorino[a,*], C.Y. Shen[a], T.E. Evans[a], G.J. Lindemann[a], Z.R. Hallock[b], L.K. Shay[c]

[a] Remote Sensing Division, Naval Research Laboratory, Code 7250, Washington, DC 20375-5320, USA
[b] Oceanography Division, Naval Research Laboratory, Stennis Space Center, Mississippi, USA
[c] Rosenstiel School of Marine and Atmospheric Sciences, University of Miami, Miami, FL, USA

Abstract

The technique of 'velocity projection' (J. Geophys. Res. 106 (2001) 6973) is used to estimate the sea-surface height field and its change over time from measurements of surface velocity made using a shore-based HF Doppler radar over a 30 × 30-km region of the continental shelf located near the mouth of the Chesapeake Bay (USA). Projected current profiles are compared with measured currents from an array of acoustic Doppler current profilers, and the consistency and sensitivity of the projections to model assumptions are also examined. Using projected values of the local surface slope, a model sea-surface $\eta(x, y)$ is least-squares fit over the study region at each measurement time. The error associated with these fits provides an internal check on the validity of the projection results. The slope of the model sea-surface shows a set-up toward the mouth of the Chesapeake Bay during downwelling-favorable winds and a counterclockwise rotation over the tidal cycle that is consistent with linear, shallow-water dynamics. A time series of sea-level difference extracted from the η maps shows a dominant M_2 tidal signal that compares well with measurements of bottom pressure made at two moorings. With proper attention to limits of applicability, such projection-based sea-surface slope fields (as well as other projection results) may be useful in diagnostic calculations or as nowcasts for use with prognostic models.
© 2003 Elsevier Ltd. All rights reserved.

Keywords: Velocity projection; Sea-surface slope; HF doppler radar; Current profiles; Nowcasts

1. Introduction

In a recent paper, Shen and Evans (2001) describe a practical technique they refer to as

*Corresponding author. Tel.: +1-202-767-3756; fax: +1-202-767-3303.
E-mail address: marmorino@nrl.navy.mil
(G.O. Marmorino).

'velocity projection' that uses measurements of sea-surface velocity and shear stress along with equations for the viscous diffusion of momentum and shear downward from the surface to infer an approximate vertical profile of the water velocity. These constraints provide vertical derivative quantities at the boundaries that are indicative of the velocity variation across the water column if

the vertical scale of this variation is comparable to the thickness of the viscous Ekman boundary layer. The technique should thus be applicable on the inner shelf, where surface and bottom Ekman boundary layers overlap. Measurements of the velocity at the surface can then be 'projected' downward to yield an approximate velocity profile over the entire water column. The use of dynamical constraints also allows the surface slope to be obtained as part of the projection through the curvature of the velocity profile at the seabed. A synopsis of velocity projection is provided in Section 2.

Investigation of the velocity projection technique is motivated by the availability of virtually continuous, high-resolution velocity measurements made using high-frequency (HF) Doppler radars. The velocity field measured by a HF radar is, nevertheless, only a surface view of the total three-dimensional current field. Below the surface, the speed and direction of the current can change significantly, as in the case of the Ekman spiral produced by a balance between the Coriolis and frictional forces. Velocity projection provides a means of inferring this change from surface data alone. Given accurate measurements, the time derivatives in the dynamical equations can be estimated using consecutive measurements of the surface velocity field so that a projection done using the latest two time steps provides essentially a nowcast of the total velocity field. An inference based solely on surface data can yield at best an approximate view of the subsurface current, but one which would otherwise be difficult to measure synoptically in situ. Such a view could be used, for example, to initialize (or be assimilated into) a prognostic model of the coastal circulation. Projection-based estimates of the sea-surface slope field (or, equivalently, maps of relative sea-surface height) might be similarly used. Additionally, projection-based nowcasts may be useful in diagnostic calculations. In a related study, de Valk (1999) uses the measured sea-surface slope field along with radar-measured velocity and empirical data (see Section 2.5) to estimate the three-dimensional current field near the outflow from the Rhine River.

In the present paper, the velocity projection technique is applied using HF Doppler radar data collected over a 30 × 30-km region of the continental shelf located near the mouth of the Chesapeake Bay (Fig. 1). The availability of in situ measurements of the current profile and of the bottom pressure are used to check the viability of the approach and its sensitivity to model assumptions, but such in situ data are not needed (nor are they used) to do the projection calculations. Sensitivity of the projections to model assumptions are also examined. The paper focuses on use of locally projected values of surface slope to calculate a sea-surface height field over the HF radar measurement domain. Our objective is to show that, under conditions when the velocity projection model may be expected to apply, a plausible sea-surface height field may be calculated. This is illustrated in Section 5.1 with sea-surface maps at two selected times and in Section 5.2 with a sequence of maps over a tidal cycle to show the hour-to-hour variability. Error estimates are derived to assess the limits of applicability of such projection-based sea-surface slope fields (as well as other projection results). While assimilation into numerical models is beyond the scope of the present paper, we will illustrate the use of projection results in a diagnostic calculation of all the terms in the kinetic energy balance equation, which includes the work done by wind and tide and the energy dissipated on the shelf, and which is also useful in checking the consistency of the projection results (Section 4.3).

2. Velocity projection

This section presents a synopsis of the Shen and Evans (2001) velocity projection method and its underlying assumptions. It also presents a slightly different formulation than used by those authors for calculating the required value of eddy viscosity.

2.1. Assumptions

In water a few tens of meters deep and over the kilometer or so horizontal scale resolved by a HF Doppler radar currents are essentially horizontal, and the vertical force balance is thus assumed to be hydrostatic. The two orders of magnitude
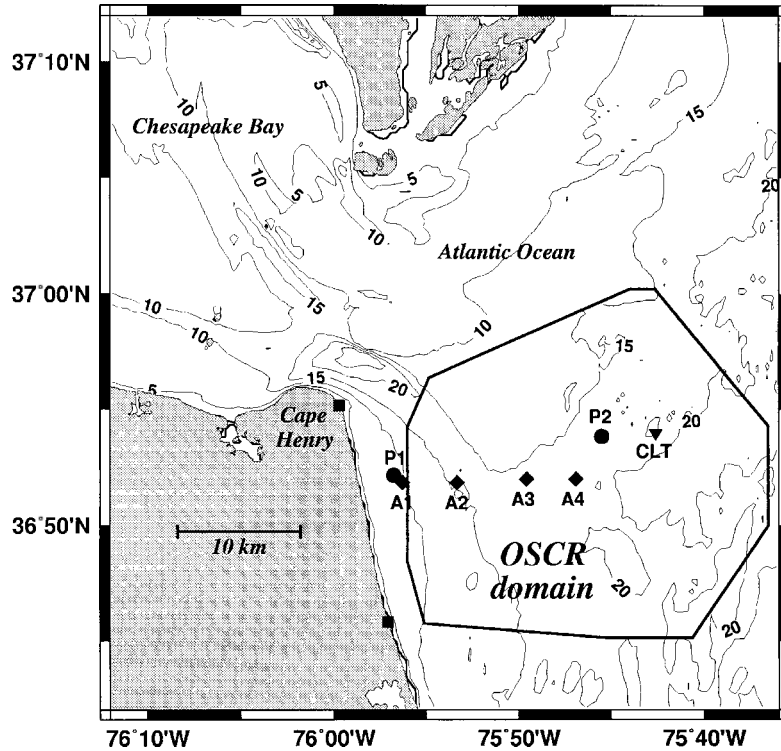
Fig. 1. Study area, showing domain of Ocean Surface Current Radar (OSCR) measurements and location of the two coastal radar installations (filled squares). Also shown are locations of ADCP moorings (A1–A4), bottom pressure moorings (P1 and P2), and the Chesapeake Light Tower (CLT). Isobaths show depth in meters.

difference between the horizontal scale and the water depth also means that momentum transfer is dominated by vertical diffusion. The momentum balance at the sea-surface is thus

$$\frac{\partial \tilde{\mathbf{u}}}{\partial t} + \tilde{\mathbf{u}} \cdot \nabla \tilde{\mathbf{u}} + \mathbf{f} \times \tilde{\mathbf{u}} = -g\frac{\tilde{\rho}}{\rho_0}\nabla \eta + v_e\left(\frac{\partial^2 \mathbf{u}}{\partial z^2}\right)_{z=\eta}, \quad (1)$$

where $\tilde{\mathbf{u}}$ is the surface velocity vector, $\mathbf{f} = (0, 0, f)$ is the Coriolis frequency ($f \approx 8.76 \times 10^{-5}\,\mathrm{s}^{-1}$); $\nabla = (\partial/\partial x, \partial/\partial y)$ is horizontal gradient operator; η is the sea-surface height, v_e is the kinematic eddy viscosity, $\tilde{\rho}$ is the surface density, ρ_0 is a constant reference density, and $\mathbf{u}$ is the horizontal velocity vector. A depth-uniform eddy viscosity model (Section 2.4) is used to assure that the velocity profile is characterized by a single vertical scale, i.e. the Ekman boundary layer thickness $\delta = (2v_e/f)^{1/2}$. The velocity profile can then be inferred

from the surface derivative quantities as shown below.

2.2. Data constraints

At the sea-surface, $z = \eta$, the projection velocity profile $\hat{\mathbf{u}}(z)$ is constrained to satisfy the measured sea-surface velocity $\tilde{\mathbf{u}}$, i.e.

$$\hat{\mathbf{u}}(z = \eta) = \tilde{\mathbf{u}} \quad (2)$$

and the surface shear is constrained by using the measured wind stress, i.e.

$$\left.\frac{\partial \hat{\mathbf{u}}}{\partial z}\right|_{z-\eta} \equiv \tilde{\mathbf{s}} = \frac{\tau_w}{\rho_0 v_e}. \quad (3)$$

An alternative in future work might be to use measurements of the vertical shear made using a multifrequency Doppler radar (e.g. Teague et al., 2001).

2.3. Dynamical constraints

At the surface, the diffusion of surface momentum is given by

$$v_{\mathrm{e}}\left(\frac{\partial^2 \hat{\mathbf{u}}}{\partial z^2}\right)_{z=\eta} = \frac{\partial \tilde{\mathbf{u}}}{\partial t} + \tilde{\mathbf{u}}\cdot\nabla\tilde{\mathbf{u}} + \mathbf{f}\times\tilde{\mathbf{u}} + g\frac{\tilde{\rho}}{\rho_0}\nabla\eta \qquad (4)$$

and the diffusion of surface shear is

$$v_{\mathrm{e}}\left(\frac{\partial^3 \hat{\mathbf{u}}}{\partial z^3}\right)_{z=\eta} = \frac{\partial \tilde{\mathbf{s}}}{\partial t} + [\tilde{\mathbf{u}}\cdot\nabla\tilde{\mathbf{s}} + \tilde{\mathbf{s}}\cdot\nabla\tilde{\mathbf{u}} - \tilde{\mathbf{s}}\nabla\cdot\tilde{\mathbf{u}}]$$
$$+ \mathbf{f}\times\tilde{\mathbf{s}} - g\frac{\nabla\tilde{\rho}}{\rho_0} \qquad (5)$$

(In the subsequent calculations, the non-linear spatial derivative terms in Eq. (5) are neglected.)

At the seabed, $z = -h$, a no-slip condition is used

$$\hat{\mathbf{u}}(z = -h) = 0 \qquad (6)$$

so that the momentum balance is between the horizontal pressure gradient and vertical momentum diffusion, i.e.

$$0 = -g\frac{\tilde{\rho}}{\rho_0}\nabla\eta - \frac{g}{\rho_0}\int_{-h}^{\eta}\nabla\rho\,dz + \left(v_{\mathrm{e}}\frac{\partial^2\hat{\mathbf{u}}}{\partial z^2}\right)_{z=-h}. \qquad (7)$$

In vertically well-mixed water, the baroclinic pressure gradient term in Eq. (7) may be approximated as

$$\frac{g}{\rho_0}\int_{-h}^{\eta}\nabla\rho\,dz \approx \frac{g}{\rho_0}(h+\eta)\nabla\tilde{\rho} \qquad (8)$$

and evaluated from the sea-surface density field (if such measurements are available). Where the baroclinic term can be neglected, $\nabla\eta$ in Eq. (7) is given solely by the curvature of the velocity profile near the bottom and hence is inferred as part of the velocity projection solution. Except for an illustrative example, all the projection results shown in this paper will ignore the baroclinic contribution and thus will be most applicable to periods of weak stratification or to areas of the measurement domain where the density gradient is small.

2.4. Eddy viscosity model

A model for the eddy viscosity is required for velocity projection. In Shen and Evans (2001), the eddy viscosity is taken to be proportional to the energy of the depth-averaged flow. The value of eddy viscosity is then determined as part of the solution procedure, providing an internal consistency. For the projection examples shown by Shen and Evans, the wind was approximately steady. In our case, the wind is variable, and initial calculations using their formulation yielded at times unrealistic near-surface shear. So, in order to represent better the wind-induced momentum exchange near the surface, we follow the formulation of Davies and Xing (2001) and express the eddy viscosity as

$$v_{\mathrm{e}} = v_{\mathrm{flow}} + v_{\mathrm{wind}} \qquad (9)$$

except that in our work each of the two contributions will be assumed to be depth-independent. In Eq. (9) v_{flow} is a flow-dependent eddy viscosity based on the depth-averaged speed and is given by

$$v_{\mathrm{flow}} = c_{\mathrm{flow}}h\langle|\hat{\mathbf{u}}|\rangle, \qquad (10)$$

where $c_{\mathrm{flow}}\approx 2.5\times 10^{-3}$ is a constant and v_{wind} is a wind-dependent eddy viscosity is given by

$$v_{\mathrm{wind}} = \kappa u_* \lambda_*, \qquad (11)$$

where $\kappa\approx 0.4$ is von Karman's constant, $u_* = |\tau_w|^{1/2}/\rho_0$ is the friction velocity, and $\lambda_*\approx O(1\,\mathrm{m})$ is a near-surface mixing length.

The value of λ_* can be expected to vary with the wind stress and characteristics of the wind-driven waves. An expression for λ_* that incorporates these effects can be derived from models of the wind-driven shear flow (e.g. Madsen, 1977 and Csanady, 1997). These models use an eddy viscosity $v = \kappa u_* z$, where z is the distance from the sea-surface. This formulation is analogous to Eq. (11) but is depth-dependent. If we can derive an appropriate mean value for v, then the corresponding mean value of z can be used to define λ_*. This can be accomplished by requiring the shear flow to have a surface speed w_{s} equal to the classical Ekman value $w_{\mathrm{s}} = u_*^2/(v_{\mathrm{Ekman}}f)^{1/2}$, where v_{Ekman} is a vertically constant eddy viscosity. Madsen (1977) used this artifice to derive values of the eddy viscosity that vary realistically with wind speed. If v_{Ekman} is substituted for v, then the results

of Madsen or Csanady can be used to write λ_* as

$$\lambda_* = \frac{l}{(\ln l/r + \kappa a)^2 + \kappa b^2},\qquad(12)$$

where $l = \kappa u_*/f$, r is a wave-related roughness length, and a and b are constants. Following Csanady (1997), r can be determined from the expression $r = 0.08\,W_s^2/g$, where W_s is the wind speed and values for a and b can be taken to be 8.5 and 10.7. With these choices, λ_* will increase to about 1 m as u_* increases to about 2.5 cm/s.

2.5. Solution method

To apply the constraints of Sections 2.2 and 2.3 at any time step and location, the velocity $\hat{\mathbf{u}}(z)$ is approximated using a set of five orthogonal functions (e.g. Chebyshev polynomials) $F_i(z)$,

$$\hat{\mathbf{u}}(z,t) = \sum_{i=0}^{4} \mathbf{c}_i(t) F_i(z),\qquad(13)$$

where $\{\mathbf{c}_i,\ i = 0, 1, 2, 3, 4\}$ is the set of unknown vector weights. The problem then is to find the values of $\mathbf{c}_i$ such that $\hat{\mathbf{u}}(z)$ and its derivatives evaluated at the boundaries satisfy the five vector kinematic and dynamical constraints represented by Eqs. (2)–(6). The time derivatives in Eq. (4) are estimated as central differences (in our case, over a 40-min interval). The non-linear terms in Eq. (4) are estimated at a particular HF Doppler radar measurement cell as central differences (over 2 km) using the four adjacent cells. Since the eddy viscosity is a function of the current speed, an iterative procedure is adopted in which the initial value of v_e is evaluated using the measured surface current in Eq. (10). The initial projected current profile is then used to make a new estimate of v_e and a new projection is done. After repeated iteration the solution eventually converges on a final value of v_e and on final u and v profiles. The calculation of the second vertical derivative of the current profile at the bottom yields the sea-surface slope $\nabla\eta$ using Eq. (7) for periods and areas when the baroclinic term is negligible. Note that this solution method differs from that used by de Valk (1999) as he used data to calibrate all the parameters in his model, including the vertical modes, which were derived from empirical ortho-

gonal function analysis of ADCP profiles. In our approach, ADCP data are not needed to do the projections.

3. Data

3.1. Background and measurements

The surface currents to be used in the velocity projection calculations were measured using the University of Miami's Ocean Surface Current Radar (OSCR) (e.g. Shay et al., 2001). Measurements were made at 20-min intervals and at a horizontal resolution of approximately 1 km. The OSCR system used an 88.5-m long, 16 element phased-array antennae to achieve a narrow beam, electronically steered over the illuminated ocean area. The beamwidth can be estimated from the radar wavelength (11.81 m) divided by array's length (e.g. Gurgel et al., 1999), which gives 0.133 rad. At a range of 30 km, this yields an azimuthal spread of about 3.7 km. As this is larger than the cell spacing, one might expect the estimates of current at far range to be spatially smoother; however, there are other factors to consider, such as an expected reduction of the signal-to-noise ratio at far range. Clearly the output from velocity projection will be sensitive to the quality of the HF radar dataset. For OSCR data, quality and noise issues have been carefully addressed in several studies (e.g. Haus et al., 1998; Shay et al., 2001).

Nearly continuous OSCR measurements are available from 27 October (day 300) through 30 November (day 333) 1997. The OSCR domain (Fig. 1) extends from the mouth of the Chesapeake Bay southward along the Virginia coast and seaward about 30 km across the inner shelf, where water depths are generally less than 20 m. Under conditions of high freshwater discharge, a mean buoyant plume (salinity $\leqslant 22$) extends to near the center of the OSCR domain (e.g. Marmorino et al., 1999), but the measurements used in the present paper were made during conditions of relatively low autumnal discharge. Consequently, the plume is expected to have a smaller influence on stratification and horizontal density gradient than

at other times of the year. Winds were measured on the Chesapeake Light Tower (Fig. 1) and converted to estimates of surface wind stress using a wind-speed-dependent drag coefficient. Both the OSCR and wind data were 6-h lowpass filtered to reduce the effect of measurement noise on the velocity projection calculations.

In situ measurements were made from day 279 through day 314 at the mooring locations shown in Fig. 1. Current profiles were measured using four acoustic Doppler current profilers (ADCPs) (Hallock and Marmorino, 2002). These were moored on the bottom along an east–west line (moorings A1 through A4). The profiles have a vertical resolution of 1 m and extend from about 2 m beneath the surface to 4 m above the bottom. Bottom pressure sensors were deployed at positions P1 (adjacent to mooring A2) and P2. The pressure data were adjusted for variations in atmospheric pressure and converted to sea-level fluctuations η. An estimate of the across-shore sea-level difference was computed as $\Delta\eta = \eta_{P1} - \eta_{P2}$. The $\Delta\eta$ record was contaminated by a number of offsets (of the order of 30 cm), which occurred during periods of high or rapidly changing winds and currents. (The offsets may have been induced in part through the motion of surface buoys that were attached to each of the pressure moorings.) Thus, the $\Delta\eta$ values are suspect at periods longer than about the tidal time scale. A conductivity-temperature recorder was deployed at 1-m depth at mooring A2, providing a record of the varying salinity over the inner shelf. A second recorder was deployed near the P2 mooring but ceased operating on day 301; over its 22-day record the surface salinity was approximately constant at 30.7 (S.D. ≈ 0.7), which is a typical shelf-water value and is thus consistent with a negligible influence of the plume at that location.

3.2. Data subset period

A period of 4 days (310–313) of coincident OSCR and in situ data was chosen for detailed study, and Fig. 2 shows an overview of the winds, salinity, and sea level data. (The bottom panel, showing the $\Delta\eta$ record, can be ignored until Section 5.1.) A variable wind forcing is expected

to modulate the effect of buoyancy. Winds during the first half of the period are primarily onshore and southward, forcing the discharge plume to lie close to the coast and resulting in weak stratification over most of the OSCR domain. This is borne out by an increasing salinity on day 310 and highest salinity (> 30) occurring on days 311 and 312. On day 313, the winds change to blow strongly southeastward, i.e. down the axis of the bay; the salinity decreases steadily, suggesting an increasing outflow from the bay and advection of the plume farther offshore. Sea levels show an increasing trend during days 310–312 and a decreasing trend on day 313.

The variability suggested by the wind and salinity records is supported by the OSCR data, a sample map from each day being shown in Fig. 3. The first three maps (Figs. 3a–c) correspond to near maximum ebb tide. On day 310 (Fig. 3a), a region of stronger flow curves anticyclonically and extends to between moorings A2 and A3. The salinity record indicates this is fresher water being discharged from the bay mouth. The flow over the bulk of the domain is relatively uniform. On day 311 (Fig. 3b), under stronger wind forcing, the flow is stronger and there is no distinct signature of a discharge. On day 312 (Fig. 3c), there is a weak current front located near mooring A3 but the salinity is still high at mooring A2, suggesting a weakly buoyant discharge and consequently relatively weak across-shelf salinity gradient. The map on day 313 (Fig. 3d) shows conditions during flood tide and strong down-bay wind forcing. There is now a large area of outflow that extends to between moorings A3 and A4. Under such conditions one suspects the horizontal density gradient will be locally large near the edge of the plume outflow.

The chosen data period is thus seen to exhibit a range of behavior that includes a varying stratification and modulation of the horizontal density gradient. Thus, the velocity projection assumptions of a depth-uniform eddy viscosity and neglect of the baroclinic pressure gradient are likely to be less applicable at some times than at others. It will, therefore, be important to devise a way of discriminating between realistic and unrealistic results.
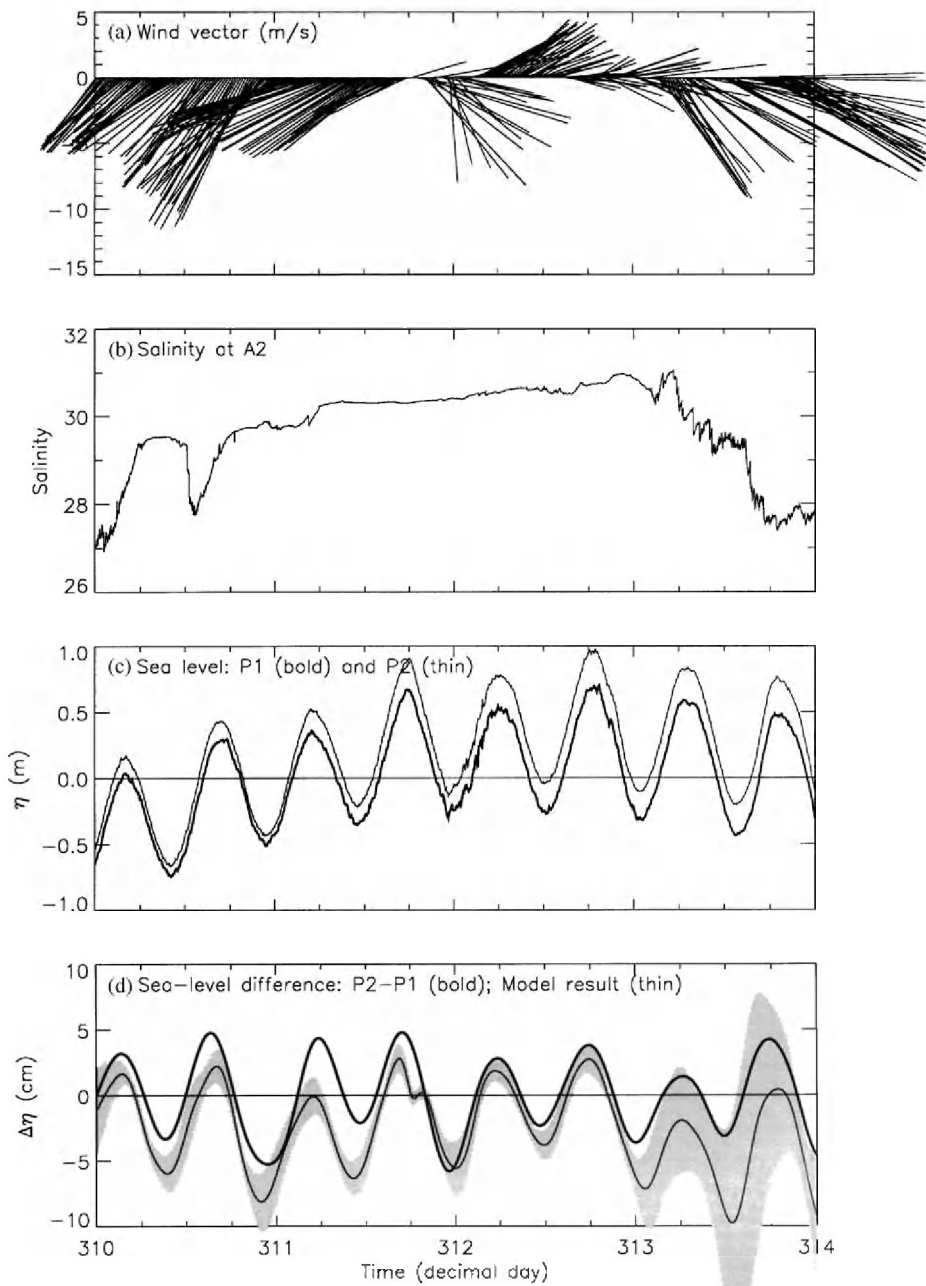
Fig. 2. Selected observations made on days 310 through 313. (a) Vector wind at CLT. (b) Near-surface salinity measured near mooring A2. (c) Sea level η at moorings P1 and P2. (d) Across-shore sea-level difference $\Delta\eta = \eta_{P1} - \eta_{P2}$, which likely shows a significant signal at only the dominant M_2 frequency (see text). The thin curve in (d) is an estimate of $\Delta\eta$ from velocity projection; the shaded region shows the approximate error, which is largest on day 313, when the stratification is greatest and the extent of the plume is largest.
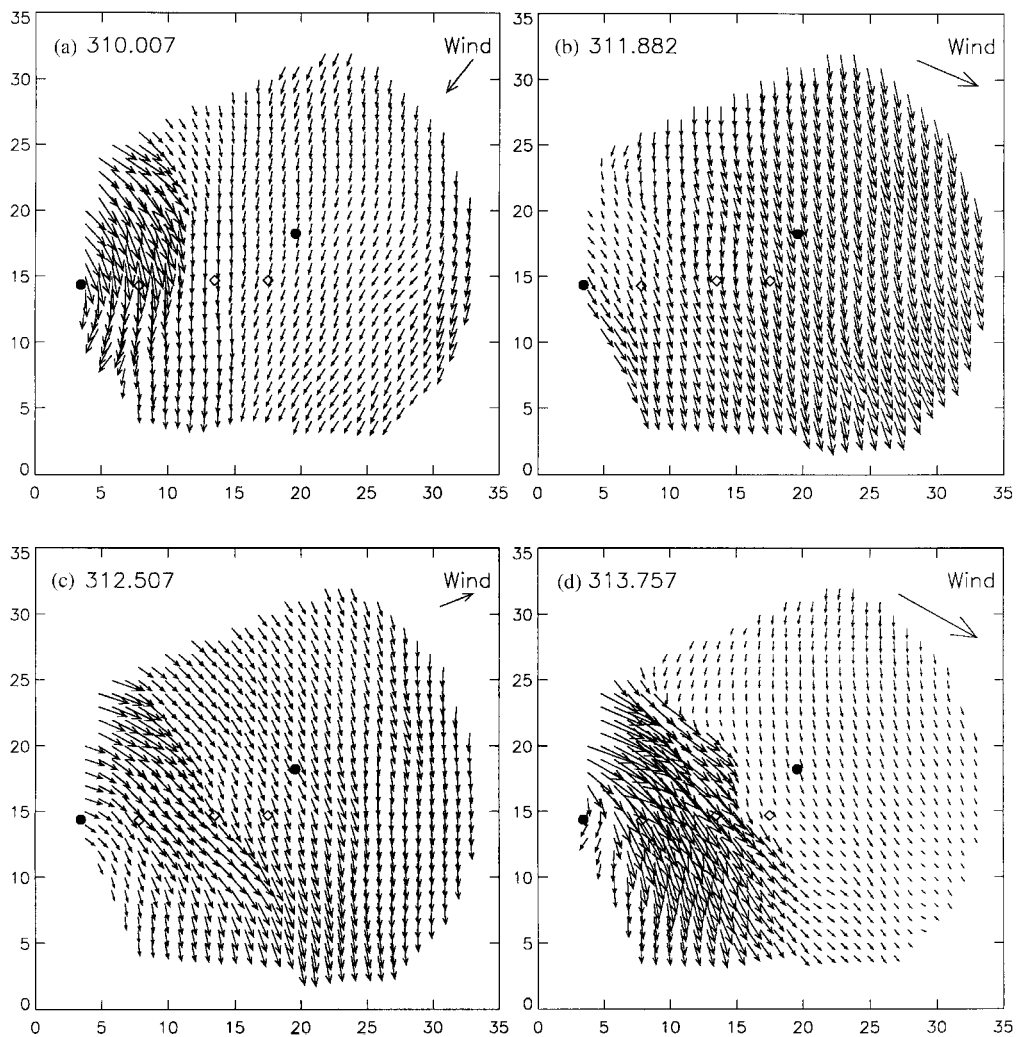
Fig. 3. Sample OSCR maps from each of 4 days in the study period: (a) 310.0, (b) 311.9, (c) 312.5, and (d) 313.8. Maps in (a–c) are during ebb tide; (d) flood tide. Axes show distances in kilometers. A current vector of 1 m/s and a wind vector of speed 10 m/s are equal in scale to a distance of 5 km. There are 686 current vectors shown in each map.

4. Velocity projections compared to ADCP data

In this first part of the results, projections are done at the OSCR cells lying closest to each of the four ADCP moorings. (The offset between the nearest cells and moorings is less than 0.5 km except for mooring A1, where the nearest useable OSCR cell lies 1.4 km to the east.) The projected profiles are then compared with the ADCP profiles as a check on the viability of the approach and to address the sensitivity of the results to model assumptions. It is important to keep in mind that the ADCP data are used here for comparison purposes only, i.e. they are not used to do the projection calculations.

4.1. Velocity sections and baroclinic effects

The projected current profiles are compared with the ADCP measurements in Fig. 4, which shows across-shelf sections of u and v components for two particular times (the same as for Fig. 3b

and d) that illustrate the range of variability in the results. The sections from day 311 (Fig. 4a) compare reasonably well. The projected u component shows an interior region of negative values (delineated by the 0-cm/s contour) similar to weakly negative values (≈ -5 cm/s) measured by the ADCPs; the projected v component shows contours that slope steeply upward toward the shore though not as steeply as in the measurements, which are nearly vertical in the figure and suggest a water column that is vertically well-mixed. Differences between the projected and

ADCP sections near the surface are small (about 5 cm/s) and lie within the expected rms differences between the ADCP and OSCR measurements (e.g. Shay et al., 2001). By way of contrast, the sections from day 313 (Fig. 4b) show a fundamental difference in the u component over the center part of the section. The ADCP measurement shows a strong flow reversal in the lower part of the water column whereas the projection shows a uniform shear flow. The comparison between v components is much better; note that the positive v values measured at mooring A1 are not reproduced in the
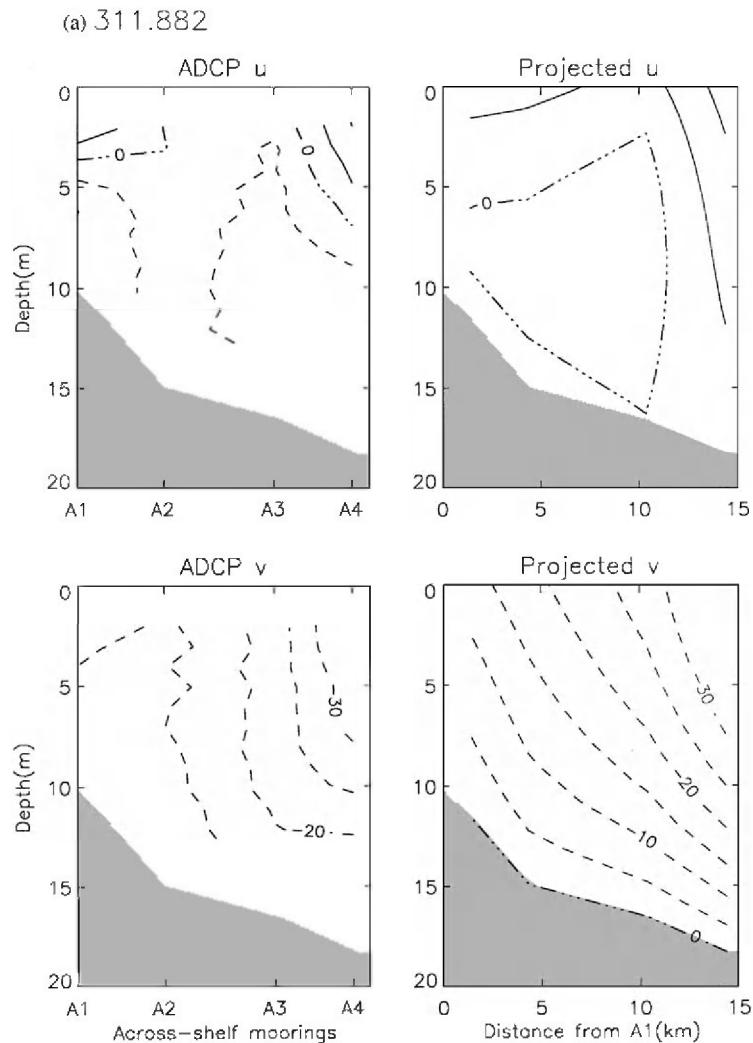

Fig. 4. Across-shelf velocity sections: ADCP measurements (left) and velocity projection (right). Contour interval is 5 cm/s. (a) Day 311.9 (same time as Fig. 3b); (b) Day 313.8 (Fig. 3d).
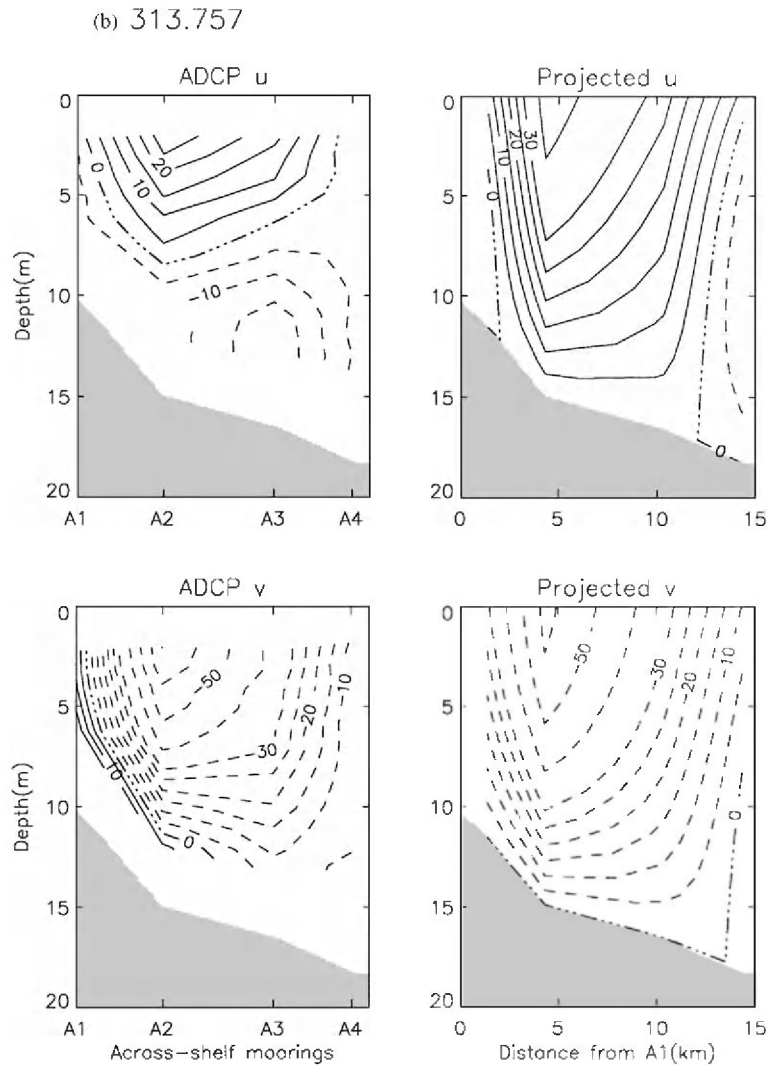
(b) 313.757

Fig. 4 (*continued*).

projection section because the calculations do not extend that far inshore.

The discrepancy in the *u* component on day 313 is likely due to the neglect of the baroclinic pressure gradient, which was likely large at this time because of the low salinity measured at mooring A2 and the strong outflow from the bay. Fig. 3d shows rather clearly at this time that the edge of the plume lies 1–2 km east of mooring A3; this is where the projected *u* in Fig. 4b breaks down. The plume edge is oriented nearly north–south, which suggests a local large horizontal density gradient oriented largely in the eastward direction. To illustrate the effect this gradient has on the calculation, the projection at mooring A3 was redone to include an *x*-component baroclinic pressure gradient. The surface density gradient was estimated using a density difference of $0.00235\,\text{kg/m}^3$ (based on the difference between the mooring A2 salinity of 27.6 and the mean offshore salinity of 30.7) divided by the distance (about 8 km) between mooring A2 and the estimated position of the plume front. We assume this gradient is independent of depth so that we

can use the approximation given by Eq. (8), in which we also assume $\eta \ll h$. The baroclinic pressure gradient term then has a value of $4.75 \times 10^{-5}\,\mathrm{m^2/s}$. Use of the revised projection profile modifies the section of u component velocity, which now shows (Fig. 5) structure near mooring A3 that more closely approximates the ADCP data. Table 1 shows the corresponding changes in the x-momentum balance terms at the surface. It can be seen that the initial force balance is approximately geostrophic, but adding the baroclinic pressure gradient changes it to one between sea level slope and friction, which is more
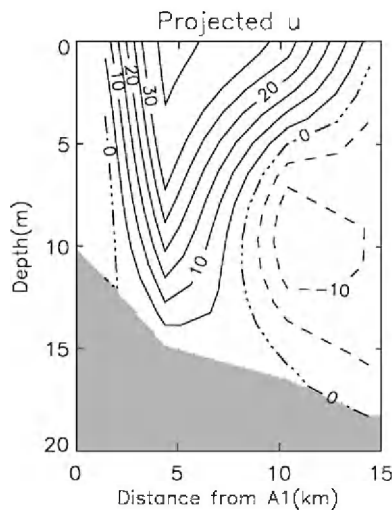
akin to non-rotational frontal dynamics. However, because the effects of vertical stratification have been neglected, the values of the slope and friction terms are too high, which is also the case for the shear and momentum diffusion terms (Eqs. (5) and (7)), which are also tabulated. Nevertheless, the calculation serves to emphasize the local importance at times of baroclinic effects. At present it is unclear how to incorporate these effects into the calculations given the very limited surface density data available in this study. Therefore, the effect of a horizontal density gradient is ignored in the remaining calculations.

4.2. Comparisons near middle of OSCR domain

Additional comparisons between projected and measured currents were done as time series at a fixed depth. A depth of $z = (2/3)h$ was chosen as being sufficiently removed from the surface data constraint and yet far enough off the bottom to overlap the available ADCP data. An example is shown in Fig. 6 at mooring A4 (local water depth of about 18 m), which, because of its central location and distance from the bay mouth, best represents the bulk of the OSCR domain. It is seen (Fig. 6a) that the projected current speed generally tracks the ADCP current speed quite well but it underestimates the measured values. This shortfall results from the use of a no-slip boundary condition and a single (viscous) depth scale, which prevents reproducing a more realistic structure in the bottom boundary layer (c.f. Fig. 4). Directional errors in the projected velocity are about $16°$ (rms). The direction error increases late on day

Fig. 5. As in Fig. 4b (u component) but including a depth-independent baroclinic pressure gradient in the calculation at mooring A3 that is based on the measured salinity difference between moorings A2 and A6.

Table 1
Comparison of values of terms for the u-component projection done near mooring A3 for (a) the standard case of zero baroclinic pressure gradient versus (b) a depth-independent value of $4.75 \times 10^{-5}\,\mathrm{m/s^2}$

Terms in surface x-momentum balance (Eq. (4))						Eq. (5)	Eq. (7)	Eq. (8)
	$\dfrac{\partial \tilde{u}}{\partial t}$	$\tilde{u}\dfrac{\partial \tilde{u}}{\partial x} + v\dfrac{\partial \tilde{u}}{\partial y}$	$-f\tilde{v}$	$g\dfrac{\tilde{\rho}}{\rho_o}\dfrac{\partial \eta}{\partial x}$	$\nu_e\left(\dfrac{\partial^2 \tilde{u}}{\partial z^2}\right)_{z=\eta}$	$\nu_e\left(\dfrac{\partial^3 \tilde{u}}{\partial z^3}\right)_{z=\eta}$	$\nu_e\left(\dfrac{\partial^2 \tilde{u}}{\partial z^2}\right)_{z=-h}$	$\dfrac{gh}{\rho_o}\dfrac{\partial \tilde{\rho}}{\partial x}$
(a)	1.78	−2.40	2.90	−1.62	0.66	0.07	1.62	0
(b)	1.78	−2.40	2.90	−82.0	−89.4	31.9	−77.3	4.75

The corresponding values of eddy viscosity derived from velocity projection are (a) $1.68 \times 10^{-2}\,\mathrm{m^2/s}$ and (b) $1.81 \times 10^{-2}\,\mathrm{m^2/s}$. All table entries have units of $10^{-5}\,\mathrm{m/s^2}$.
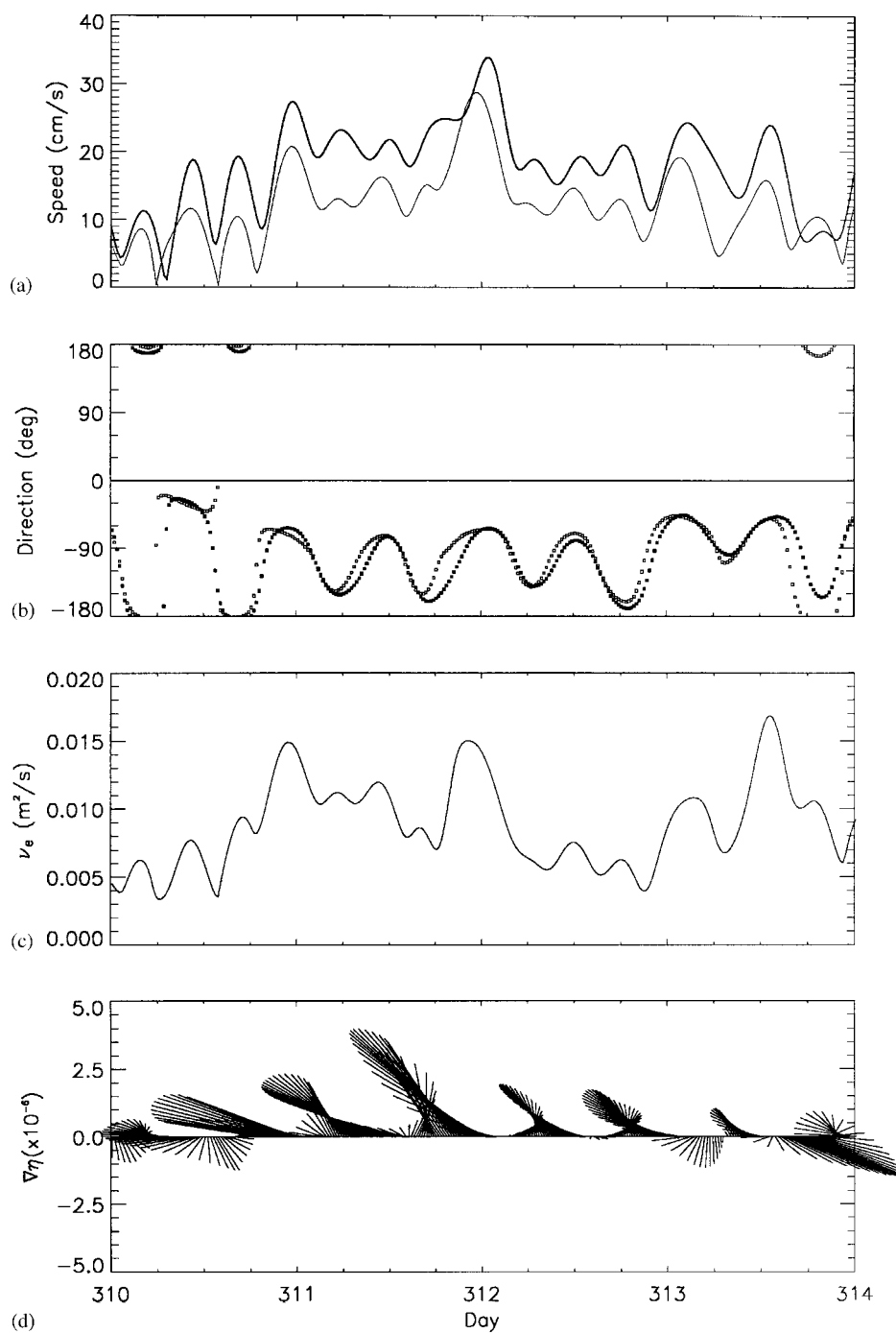
Fig. 6. Time series of projection results at mooring A4. (a, b) Current speed (thin curve) and direction (unfilled symbol) at 11-m depth, (c) eddy viscosity ν_e, and (d) $\nabla\eta$. Bold curve in (a) and filled symbol in (b) show ADCP data. Current direction is measured positive counterclockwise from east.

313, which is the time of the poor u-component comparison in Fig. 4b. Directional differences between OSCR and near-surface ADCP velocity measurements can be as large as 20° (Shay et al., 2001); thus some part of the rms error we observe may be related to measurement error in the surface data constraint.

Also shown in Fig. 6 are the projection values of the eddy viscosity and sea-surface slope. The mean value of v_e of the period is about $0.01\,\mathrm{m}^2/\mathrm{s}$. Using this value, the Ekman boundary layer thickness δ is about $15\,\mathrm{m}$, which is comparable to the local water depth and so is consistent with the model assumption. The time series of $\nabla\eta$ (Fig. 6d) is strongly modulated at the M_2 tidal period. A close examination shows a predominance of counter-clockwise rotation over time of the $\nabla\eta$ vector (see later Section 5.2). Over time scales longer than tidal, on days 311–312, biases in the $\nabla\eta$ signal are evident and these are likely induced by the wind forcing (see later Section 5.1).

4.3. Internal consistency and sensitivity of the projection results

Because the velocity projection technique uses the momentum equations as a constraint only at the sea-surface and bottom, there is a question about how well the interior momentum balance is satisfied, i.e. whether the inferred velocity profile is internally consistent with the model. This can be addressed by examining the depth-integrated balance of horizontal kinetic energy, $KE \equiv (1/2)(u^2 + v^2)$, which can be obtained by taking the dot product of $\mathbf{u}$ with Eq. (1) and integrating over the water depth. The balance is

$$\frac{\partial}{\partial t}\overline{KE} + \nabla\cdot\overline{\mathbf{u}KE} = -g\,\overline{\mathbf{u}\cdot\nabla\eta} + \tilde{\mathbf{u}}\cdot\boldsymbol{\tau}_{\mathbf{w}} - \bar{\varepsilon}, \qquad (14)$$

where the overbar indicates a vertical integration from $z = -h$ to η. The two terms on the left-hand side are the local rate of change of kinetic energy and the horizontal divergence of the flux of kinetic energy, which derives directly from the non-linear term in the momentum equation. The three terms on the right-hand side represent the rate of work done by the sea-surface gradient; the rate of work done by the wind stress, where $\tilde{\mathbf{u}}$ is the surface

velocity as before; and the depth-integrated rate of dissipation of the kinetic energy, which is given by

$$\bar{\varepsilon} = v_e \overline{\left[\left(\frac{\partial u}{\partial z}\right)^2 + \left(\frac{\partial v}{\partial z}\right)^2\right]}. \qquad (15)$$

Fig. 7 shows a time series of each of the terms in Eq. (14) evaluated using the projection results at mooring A4. The residual, representing any imbalance between the left- and right-hand sides of the equation, is generally very close to zero and small compared to the individual terms. This is evidence that the projection results are internally consistent. The reasoning is that the projected velocity profile is assumed to approximate the Ekman flow and is thus expected to satisfy approximately the time-dependent shallow-water governing equations (c.f. Eq. (1)). Had Fig. 7 exhibited a gross imbalance, the inferred flow clearly would be inconsistent with the assumed Ekman dynamics. Also note that the flux term shows significant variability, at times (e.g. at day 312.0) surpassing the local rate-of-change term, which is evidence that the non-linear term in the momentum equation can contribute significantly in determining the projected velocity profile (see also Table 1). Aside from these issues, the temporal evolution of the terms in Eq. (14) is of interest in diagnosing changes in the partitioning between pressure versus wind work and large variations in the depth-integrated dissipation. The dissipation tends to follow the wind work but is punctuated by large pressure-work events. Also, the dissipation is modulated at twice the M_2 frequency (i.e. the M_4 harmonic), with local maxima tending to coincide with maxima in current speed (c.f. Fig. 6a); however, the dissipation depends on more than the local speed as can be seen by comparing the periods with low and high dissipation values but comparable speeds, e.g. compare times 311.5 and 312.5 in Figs. 6a and 7.

Another issue concerns the sensitivity of a projection to parameters used in the eddy viscosity model (Section 2.4). (Sensitivity to measurement noise and other factors is addressed by Shen and Evans, 2001.) To examine this, the calculations were redone by changing the relative contributions of the flow- and wind-based terms in Eq. (9) by a
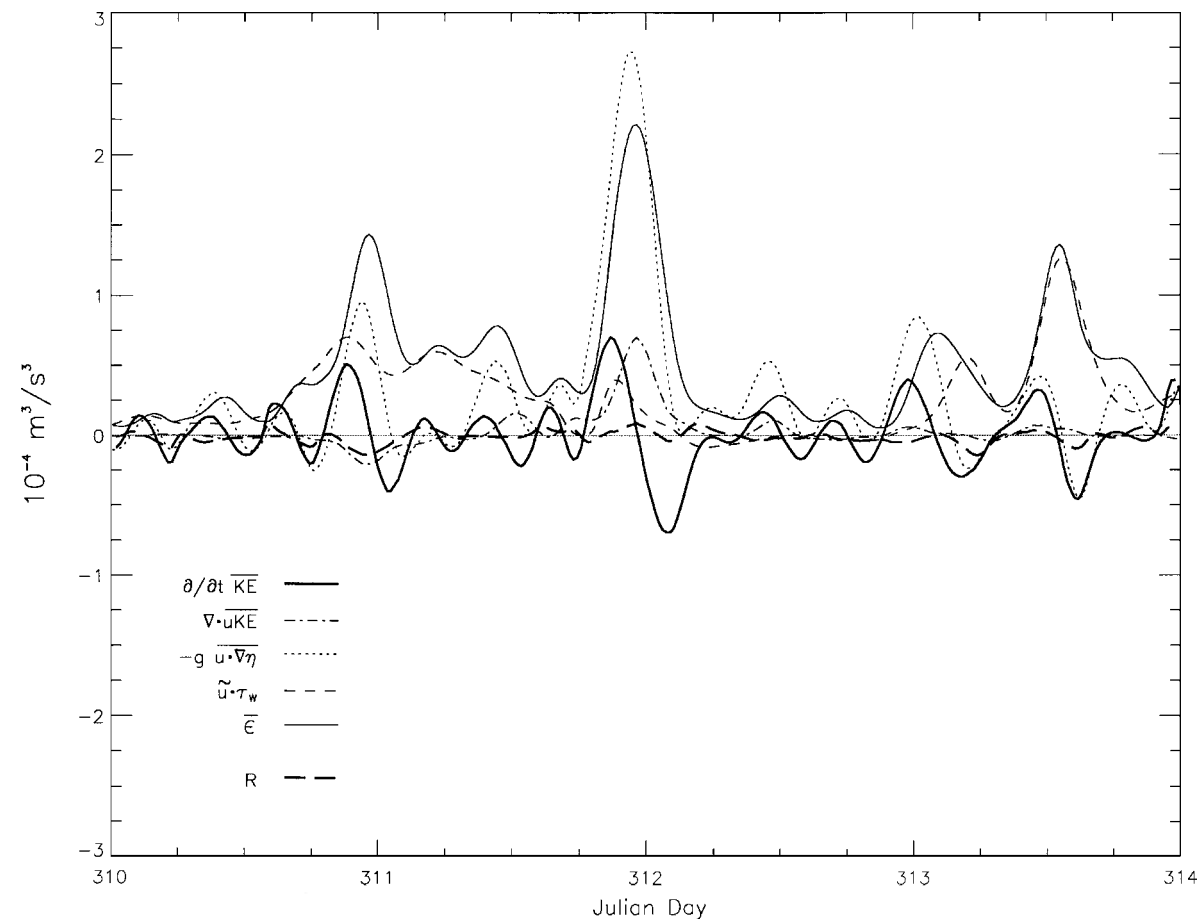
Fig. 7. Time series of terms in the horizontal kinetic energy balance (Eq. (14)) calculated from projection done at mooring A4. The residual, R, represents any imbalance between the left- and right-hand sides of Eq. (14).

Table 2
Sensitivity of projection results to factor-of-two changes in the relative contribution of the two terms in the eddy viscosity model (Eq. (9))

Case	Formulation	rms differences from measured current	
		Speed (cm/s)	Direction (deg)
1.	$v_e = \frac{1}{2} v_{flow} + v_{wind}$	7.65	23.1
2.	$v_e = 2 v_{flow} + v_{wind}$	6.23	15.2
3.	$v_e = v_{flow} + \frac{1}{2} v_{wind}$	7.12	17.4
4.	$v_e = v_{flow} + 2 v_{wind}$	6.46	15.4
Standard	$v_e = v_{flow} + v_{wind}$	6.84	15.8

Listed are root-mean-square (rms) differences from the measured current at 11-m depth at mooring A4.

factor-of-two. (This factor is larger than the expected uncertainty in the parameters and so represents an extreme test of sensitivity.) Table 2 summarizes the effect on speed and direction of the projected current at mooring A4: modifying the formulation to increase the eddy viscosity

(through either the flow or wind terms) leads to a slightly better comparison with the ADCP measurements; but a decrease in either of the eddy viscosity terms has a worsening effect particularly on the current direction. Fig. 8 shows the effect on other projection results: the final (iterated) value of eddy viscosity, and the values of sea-surface slope and dissipation. Overall, these results are least sensitive to variations in the wind-based term, most sensitive to the flow-based term. The least sensitive quantity overall is the sea-surface slope, while the vertically averaged dissipation can vary by as much as a factor-of-four for similarly large changes in the wind-based eddy viscosity term. Fig. 8 also shows that despite the large changes in viscosity values, the temporal variation of the projected quantities remains qualitatively similar.

5. Sea-surface height field

In situ measurement of coastal sea-surface slopes over scales of several kilometers is difficult except with pressure sensors deployed at selected locations. But, by combining the OSCR data with velocity projection, the surface slope can be estimated in a fairly straightforward manner as indicated in Section 2.3. In the present section, we illustrate how such estimates of the slope field can used to derive maps of surface height anomaly.

5.1. Sea-surface height anomaly maps

The starting point is to do projections at a given time step over all possible measurement cells to provide estimates of the sea-surface slope $\nabla\eta$. As estimation of the non-linear terms requires adjacent cells along the x and y directions, projections could not be done at cells lying on the boundary of the OSCR domain. As projections could not be done along boundary cells, the slope field is calculated over a slightly reduced domain compared with the current vector maps shown in Fig. 3. With the slope field determined, a model sea-surface $\eta(x,y)$ was least-squares fit so as to minimize the error over the spatial domain between the local surface gradient, $(\nabla\eta)_{\text{fitted surface}}$, say, and the local projected value of $\nabla\eta$. An

additional constraint is that the spatial mean of the η values be zero at each time step; thus contour maps of the η values portray the spatial structure or patterns of height fluctuations or anomalies rather than an absolute sea-surface elevation. Mathematically, η is determined from the following equations:

$$(\eta(i+1,j)-\eta(i-1,j))/2\Delta - \partial\eta/\partial x(i,j) = 0, \quad (16a)$$

$$(\eta(i,j+1)-\eta(i,j-1))/2\Delta - \partial\eta/\partial y(i,j) = 0, \quad (16b)$$

$$\Sigma\eta(i,j) = 0, \quad (16c)$$

where (i,j) is the cell number and Δ is the cell separation distance. The calculation represents an over-determined problem because there are N cells at which to calculate a value of η but $2N$ values of the local η spatial derivatives that need to be satisfied. In order to solve the equations, then, the we seek to minimize the objective function $\sum \{[\text{Eq. (16a)}]^2 + \text{Eq. (16b)}]^2\}$ under the constraint Eq. (16c), i.e. that the mean surface height is zero.

Associated with each fitted surface is an overall residual error $\varepsilon_{\text{residual}}$. Fig. 9 (dashed curve) shows how the residual error varies over time as compared to the spatial rms sea-surface slope $\sigma_{\nabla\eta}$ (the solid curve). The residual error is relatively small ($\approx 20\%$) on days 311 and 312, but it becomes large ($>50\%$) early on day 310 and again on day 313, periods when the measured salinity is lowest. Thus, there is a substantially larger residual error and poorer overall fit at times when the plume is more dominant (see below).

Two sample η maps are shown in Fig. 10. These correspond in time to the velocity maps shown in Fig. 3b (day 311) and in Fig. 3d (day 313). Also shown are corresponding maps of a local relative error, which is computed as $\varepsilon_{\text{relative}} \equiv |(\nabla\eta)_{\text{fitted surface}} - (\nabla\eta)_{\text{projected}}|/\sigma_{\nabla\eta}$. This relative error provides a check of the consistency of the projection result from one cell to the next. Because the calculation of a η surface is an over-determined problem, the errors associated with a fitted surface will be small only if the local projections of $\nabla\eta$ are consistent from one cell to another. The velocity projection model is a local one, and it tries to produce a current profile consistent with the locally measured time rate of change. The
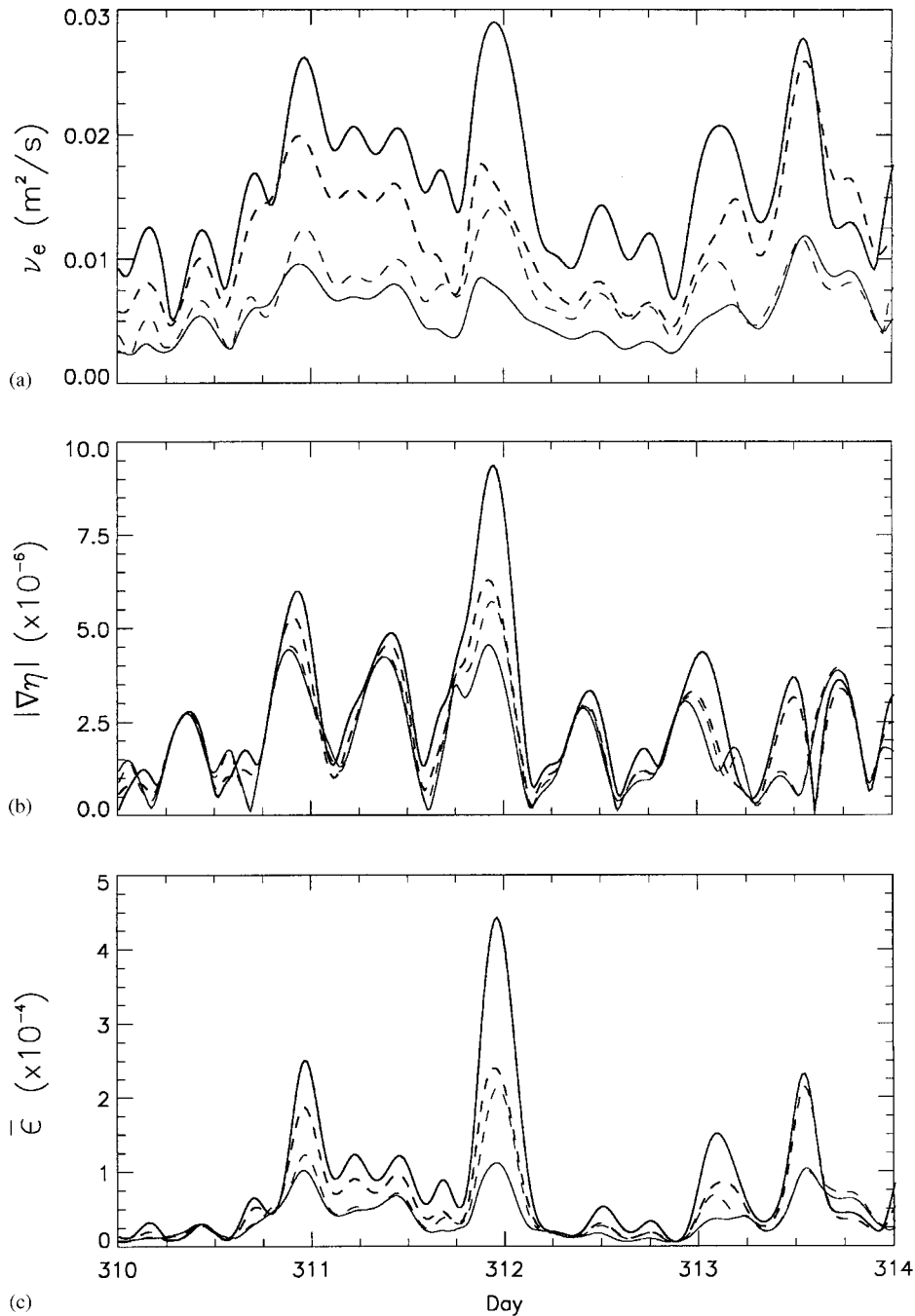
Fig. 8. Sensitivity of projection-based results to factor-of-two changes in the relative contribution of the terms in the eddy viscosity model (Eq. (9)). (a) eddy viscosity v_e; (b) sea-surface gradient magnitude $|\nabla \eta|$; (c) depth-integrated dissipation rate $\bar{\varepsilon}$. Thin solid curve: $v_e = 1/2 v_{\text{flow}} + v_{\text{wind}}$; thick solid curve: $v_e = 2 v_{\text{flow}} + v_{\text{wind}}$; thin dashed curve: $v_e = v_{\text{flow}} + 1/2 v_{\text{wind}}$; thick dashed curve: $v_e = v_{\text{flow}} + 2 v_{\text{wind}}$. Results are based on projections done at mooring A4.
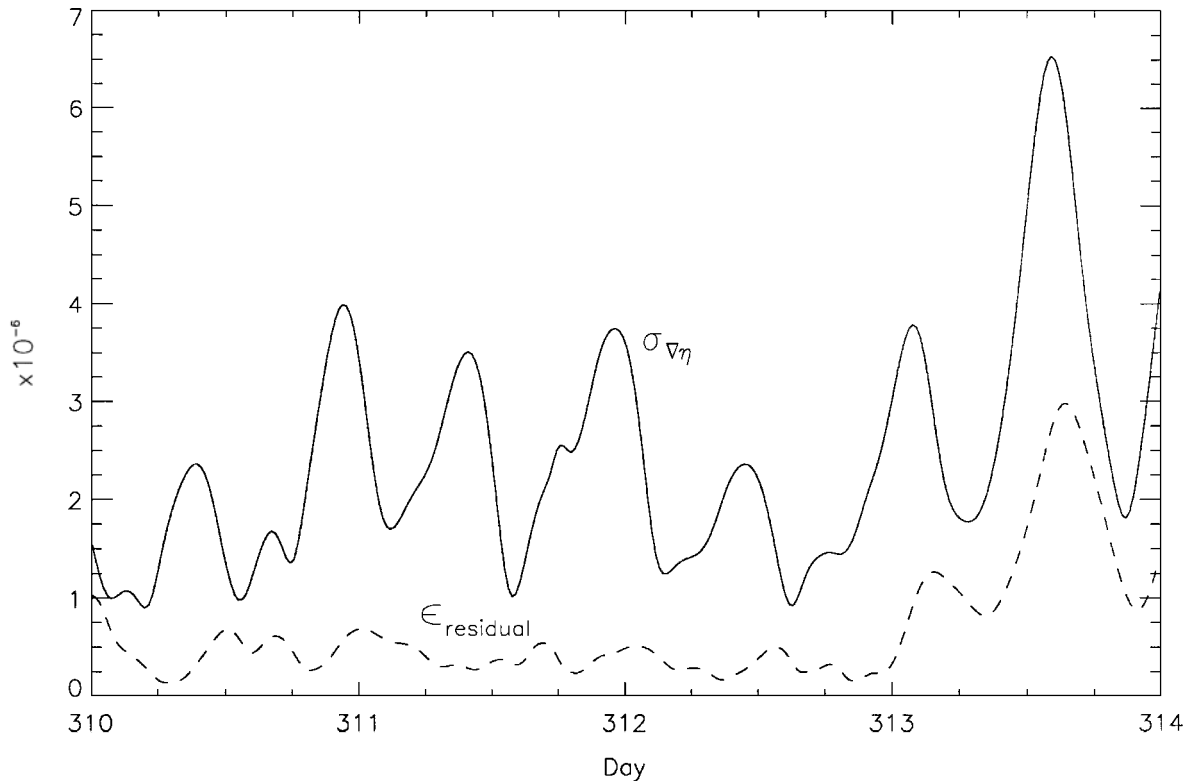
Fig. 9. Time series of rms sea-level gradient $\sigma_{\nabla\eta}$ (solid curve) computed over the OSCR domain and the residual error $\varepsilon_{residual}$ (dashed curve) in fitting a surface of sea-level height anomaly to the $\nabla\eta$ values at each time step.

projection result will thus be consistent from cell-to-cell only if the model assumption of homogeneous Ekman dynamics is correct at each cell location. Thus, the error maps provide a diagnostic for the applicability of the projection results. The error map on day 313 (Fig. 10d) shows relative errors of 0.2–0.8 in the eastern half of the OSCR domain and increasing large errors (as high as 2.2) in the western half, corresponding approximately to the area of the plume (c.f. Fig. 3d). This is an extreme case that illustrates contamination from the disparate dynamics between the plume and offshore regions.

On the other hand, the error map for day 311 (Fig. 10c) shows relative errors of less than 0.2, which tend to occur uniformly over the entire domain; thus we have some confidence in the corresponding η map. The η map (Fig. 10a) shows an approximately linear increase in sea-surface height from the southeast corner of the domain

toward the northwest; i.e. a set-up of sea level toward the bay mouth. The total change in η is about 12 cm, which gives a mean slope across the entire OSCR domain of about 5×10^{-6}. This is consistent with the value of $\nabla\eta$ determined at mooring A4 at this time (Fig. 6d). The corresponding velocity map (Fig. 3b) shows that the flow is toward the south-southeast and rotated only about 25° clockwise from being down the gradient in η. This accounts for the large pressure-work contribution at this time in the balance of kinetic energy (Fig. 7). On the other hand, the flow is rotated significantly (about 50° clockwise) from the downwind direction, so the wind-work term is relatively small. Such a diagnosis of the flow field can help sort out the effects of mean wind and sea-surface slope at a particular time step.

From the η maps such as in Fig. 10, a sea-level height difference $\Delta\eta$ was extracted at each time step using the OSCR cells closest to moorings P1
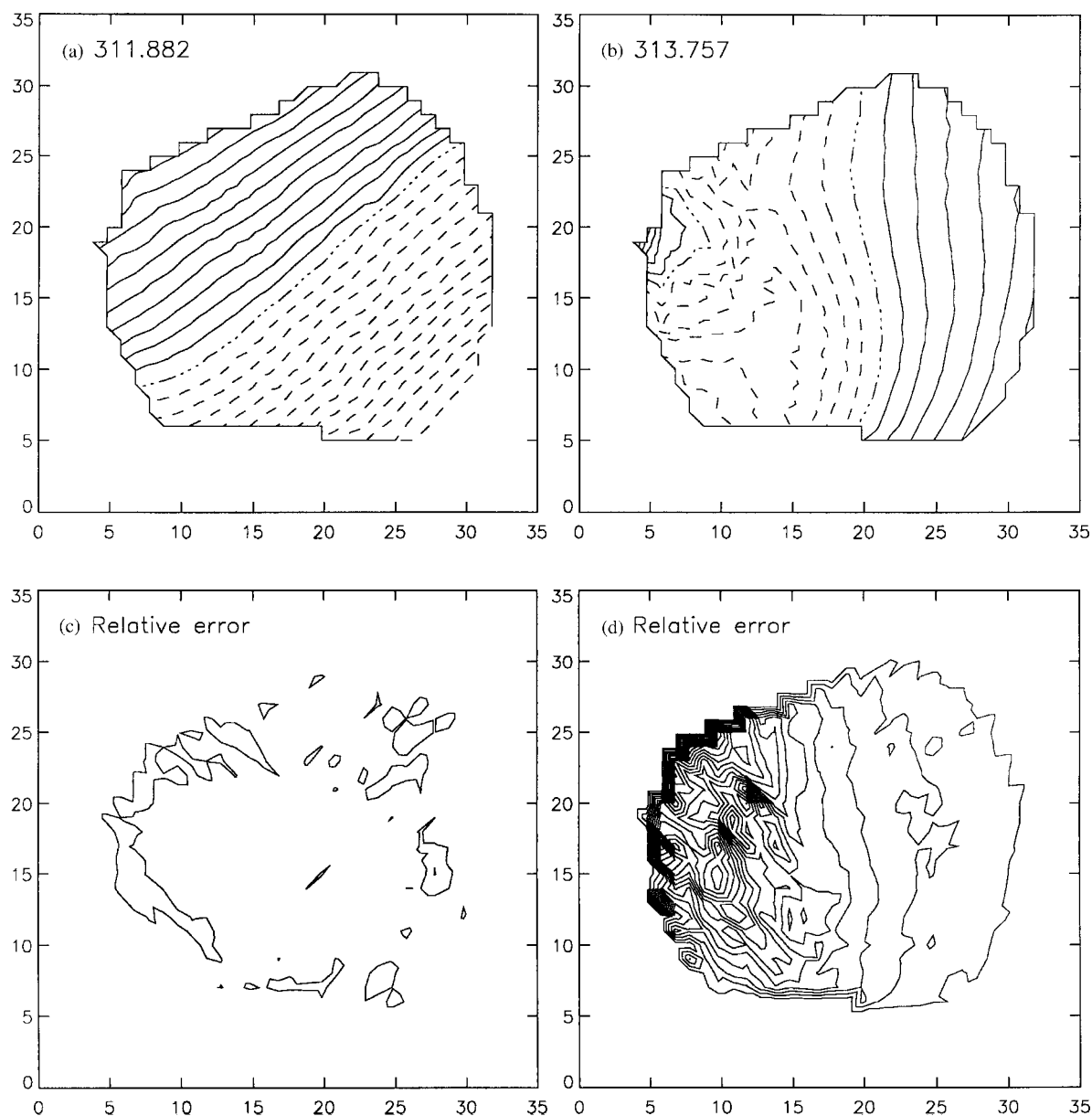
Fig. 10. (a, b) Maps of fitted sea-level height anomaly for 311.882 and 313.757. Solid (dashed) contours show positive (negative) height anomaly at intervals of 0.5 cm.(c, d) Corresponding maps of relative error. Minimum contour is 0.20; interval is 0.20. In (d), errors increase to a maximum of 220% in the western part of the OSCR domain (see text).

and P2. This signal is shown as the thin curve in Fig. 2d. Also shown is an estimate of the error, which is computed using the mean relative error averaged between the P1 and P2 locations. The projection-based $\Delta\eta$ time series contains a clear

tidal signal that compares fairly well with the observed sea-level differences at the M_2 tidal frequency. The projected $\Delta\eta$ series also shows daily means that are offset from zero. These offsets are plausibly related to wind-induced sea-level

set-up. For example, there is a large negative offset (i.e. set-up toward the bay mouth) on day 311 during a period of strong southwestward winds, a relaxation after the onset of northeastward winds on day 312, and a negative offset again on day 313 (though the error bars are quite large) during strong southeastward winds. This behavior is generally consistent with observations made by Valle-Levinson et al. (2001) who show set-up of sea level near the mouth of the bay under steady southwestward or southeastward winds and set-down under steady northeastward winds. The error bars in $\Delta\eta$ are so large on day 313 because $\Delta\eta$ is calculated across the part of the η map having relative errors in excess of 0.8 (Fig. 10d). However, near the position of mooring A4, Fig. 10d shows a relative error of somewhat less than 0.8, and Fig. 6 shows reasonable projected profiles at that location. This suggests that a relative error in a η map of about 0.8 may be used as an acceptance/rejection threshold for the projection results in the present dataset.

5.2. Sea-surface height maps over a tidal cycle

Animations of the η maps were also examined. An animation for day 312, for example, overlain with the simultaneous OSCR velocity vectors can be viewed at http://rsd-www.nrl.navy.mil/7250/CapeHenry.html. An interesting feature that appears in the animations is a tendency for relative highs and lows in sea level to rotate counterclockwise around the domain during nearly every tidal cycle. This can be shown more clearly by simply subtracting the daily mean at each cell location as this serves to remove much of the non-tidal part of the signal. A sequence of these maps from day 312 is shown in Fig. 11. There are 12 maps at hourly intervals to show one M_2 tidal period. Alongside each map is shown the corresponding velocity map (less its daily mean). While the sea-level patterns can be seen to move around the domain in a counterclockwise fashion, most of the current vectors rotate clockwise over time. Such opposing rotations are theoretically possible as long as the shape of the tidal ellipse satisfies a particular set of conditions, which were derived by Defant (1961, p. 324ff).

We have put Defant's arguments in modern notation in an appendix. Assuming linear, inviscid, shallow-water dynamics, then there is a range of parameters where the tidal velocity vector W can rotate clockwise while the tidal $\nabla\eta$ vector rotates counterclockwise. With $f > 0$ (northern hemisphere), this range is given by

$$\frac{|\sigma - f|}{\sigma + f} < \frac{|W^+|}{|W^-|} < 1, \tag{17}$$

where σ is the frequency of a particular tidal component, and W^+ and W^- are the counterclockwise and clockwise rotating components of the vector W. For the M_2 tide $\sigma = 1.41 \times 10^{-4}\,\text{s}^{-1}$, and the left-hand quantity in Eq. (17) is equal to 0.23 for our study area. Values for W^+ and W^- at mid-water depth near mooring A4's location are 7.6 and 10.9 cm/s (Shay et al.(2001); their Table 2), so that the ratio of current components is 0.70. Thus, the relationship above is clearly satisfied: $0.23 < 0.70 < 1$. The counterclockwise rotation in the maps of surface height is thus physically plausible.

6. Summary

The technique of 'velocity projection' has been applied using a dataset of HF Doppler radar measurements made over a region of the continental shelf located near the mouth of the Chesapeake Bay. The value of the projection technique is that it can provide estimates of the velocity profile over a large spatial area when in situ measurements are not available. The only data required are the radar-measured surface velocity and the wind, which was measured in this study at tower located near the center of the study area. However, newer radar systems appear to be capable of measuring the wind stress and, in addition, the spatial distribution of near-surface shear; and this would allow all the terms in the shear diffusion equation (Eq. (5)) to be calculated from radar data alone. It has been shown that the projected current profile (Figs. 4 and 6) as well as the sea-level slope inferred as part of the velocity projection (Fig. 2d) compare reasonably well with in situ measurements made in an across-shelf array
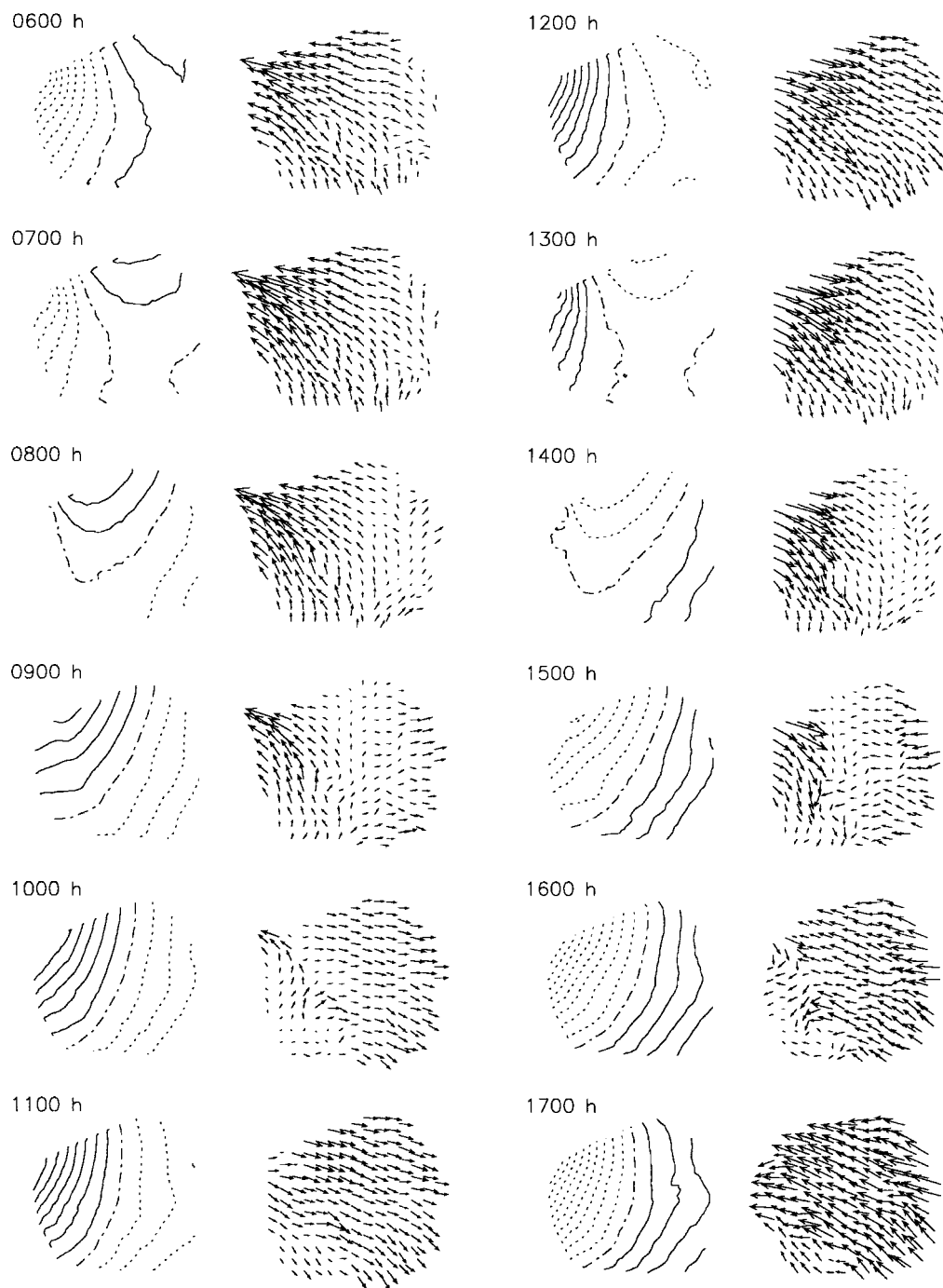
Fig. 11. Maps of η and OSCR velocity shown at 1-h intervals on day 312. Maps show fluctuations about (daily) mean values at each cell. Contour interval is 0.5 cm. Vectors are decimated by 50% for clarity. The first and last time steps correspond to near maximum flood tide.

of moored acoustic Doppler current profilers (ADCPs) and bottom pressure sensors. The projection results have been shown to be robust in that they are relatively insensitive to the details of the constant-eddy viscosity formulation used in the present version of the projection model (Fig. 8; Table 2).

Using the projected values of the local surface slope computed at individual radar measurement locations, a model sea-surface $\eta(x, y)$ was least-squares fit over the computation domain at each measurement time. The error associated with these fits provides an internal check on the validity of the projection results. Examples of these η maps show a sea-surface height field (Fig. 10a) that slopes upward toward the mouth of the Chesapeake Bay, consistent with the generally down-welling-favorable winds, and a tidally varying field (Fig. 11) in which the sea-surface slope field rotates counterclockwise with time (while the current vector rotates clockwise), which is consistent with linear, shallow-water dynamics. The surface slope field would also be of use in a diagnosis of the kinetic energy balance (e.g. Fig. 7), which allows seeing at any instant the relative importance of work done by the wind versus tides or identifying significant events and areas of kinetic energy dissipation.

Wind-forced episodes of enhanced outflow of buoyant water from the Chesapeake Bay result in periods when the model assumptions of vertically well-mixed water and depth-constant eddy viscosity are less tenable and when the baroclinic pressure gradient may be of importance. We have shown an example of how baroclinicity can be incorporated and how patterns in the HF currents can help to estimate these effects. This leads to a revised projected current profile that better matches the ADCP profile (Fig. 5), but the proper inclusion of such effects represents an area where refinement of the velocity projection technique is needed. An improvement would be to use a physically realistic representation of the plume's spatial structure and to augment the eddy viscosity model to include the effect of stratification, and methods for doing this are under investigation. Then, as better surface density data becomes available they can be incorporated into the projection technique in a rigorous manner. In situations where the water depth is greater than the Ekman layer depth, it should also be possible to apply dynamic constraints to the entire water column, as described in Shen and Evans (2002), to obtain the current profile, as opposed to relying on surface dynamic constraints alone

Acknowledgements

Appendix A. Rotation of tidal current and surface gradient vectors

For a single tidal constituent of frequency σ and velocity (U, V), define

$$W = U + iV = W^+e^{i\sigma t} + W^-e^{-i\sigma t}, \qquad (A.1)$$

where W^+, W^- are the CCW, CW (counter- and clockwise) rotating components. Assuming linear, barotropic shallow-water dynamics, we can relate the surface height η with

$$W_t + ifW = -gA = A^+e^{i\sigma t} + A^-e^{i\sigma t}, \qquad (A.2)$$

where $A \equiv \eta_x + i\eta_y$. Substitution of Eq. (A.1) into Eq. (A.2) yields:

$$A^+ = \frac{-iW^+}{g}(\sigma + f), \qquad (A.3)$$

$$A^- = \frac{iW^-}{g}(\sigma - f).$$

$|W^+| - |W^-| > 0$ implies CCW rotation while $|W^+| - |W^-| < 0$ implies CW rotation; likewise

G.O. Marmorino et al. / Continental Shelf Research 24 (2004) 353–374

for A. But, assuming $f > 0$ (northern hemisphere),

$$|A^+| - |A^-| = \frac{1}{g}(|W^+|(\sigma + f) - |W^-(\sigma - f)|) \quad (A.4)$$

and there is a range of parameters where W can rotate CW while A rotates CCW. This range is given by

$$\frac{|\sigma - f|}{\sigma + f} < \frac{|W^+|}{|W^-|} < 1. \quad (A.5)$$

For σ near or less than f the range broadens to allow all values of W^+/W^- less than 1. As σ becomes much larger than f the ranges closes to zero, i.e. W can then only rotate CCW with A.

For CW rotation of A, only CW rotation of W is possible. In this case,

$$\frac{|W^+|}{|W^-|} < \frac{|\sigma - f|}{\sigma + f} < 1. \quad (A.6)$$

References

Csanady, G.T., 1997. The slip law of the free surface. Journal of Oceanography 53, 67–80.

Davies, A.M., Xing, J., 2001. The influence of eddy viscosity parameterization and turbulence energy closure scheme upon the coupling of tidal and wind induced currents. Estuarine, Coastal and Shelf Sciences 53, 415–436.

Defant, A., 1961. Physical Oceanography, Vol. 2. Pergamon Press, Oxford, 1961, 598pp.

de Valk, C.F., 1999. Estimation of 3-D current fields near the Rhine outflow from HF radar surface current data. Coastal Engineering 37, 487–511.

Gurgel, K.W., Essen, H.H., Kingsley, S.P., 1999. High-frequency radars: physical limitations and recent developments. Coastal Engineering 37, 201–218.

Hallock, Z.R., Marmorino, G.O., 2002. Observations of the response of a buoyant estuarine plume to upwelling-favorable winds. Journal of Geophysical Research, 107, Art. No. 3066.

Haus, B.K., Graber, H.C., Shay, L.K, 1998. Ocean surface current observations with HF Doppler radar during the Chesapeake Outflow Plume Experiment, Technical Report, RSMAS, Univ. Miami, Miami FL 33149, 66pp.

Madsen, O.L., 1977. A realistic model of the wind-induced Ekman boundary layer. Journal of Physical Oceanography 7, 248–255.

Marmorino, G.O., Shay, L.K., Haus, B.K., Handler, R.A., Graber, H.C., Horne, M.P., 1999. An EOF analysis of HF Doppler radar current measurements of the Chesapeake Bay buoyant outflow. Continental Shelf Research 19, 271–288.

Shay, L.K., Cook, T.M., Hallock, Z.R., Haus, B.K., Graber, H.C., Martinez, J., 2001. The strength of the M_2 tide at the Chesapeake Bay mouth. Journal of Physical Oceanography 31, 427–449.

Shen, C.Y., Evans, T.E., 2001. Surface-to-subsurface velocity projection for shallow water currents. Journal of Geophysical Research 106, 6973–6984.

Shen, C.Y., Evans, T.E., 2002. Dynamically constrained projection for subsurface current velocity. Journal of Geophysical Research 107 (C11), Art. No. 3203.

Teague, C.C., Vesecky, J.F., Hallock, Z.R., 2001. A comparison of multifrequency HF radar and ADCP measurements of near-surface currents during COPE-3. IEEE Journal of Ocean Engineering 26, 399–405.

Valle-Levinson, A., Wong, K.-C., Bosley, K.T, 2001. Observations of the wind-induced exchange at the entrance to Chesapeake Bay. Journal of Marine Research 59, 391–416.